

## The Stability of Irradiation-Induced Defects in Zr<sub>3</sub>AlC<sub>2</sub>, Nb<sub>4</sub>AlC<sub>3</sub> and (Zr<sub>0.5</sub>,Ti<sub>0.5</sub>)<sub>3</sub>AlC<sub>2</sub> MAX Phase-Based Ceramics

Bowden, David; Ward, J.; Middleburgh, Simon; de Moraes Shubeita, S.; Zapata-Solvas, E.; Lapauw, T.; Vleugels, J.; Lambrinou, K.; Lee, Bill; Preuss, Michael; Frankel, Philipp

**Acta Materialia**

DOI:

[10.1016/j.actamat.2019.10.049](https://doi.org/10.1016/j.actamat.2019.10.049)

Published: 15/01/2020

Publisher's PDF, also known as Version of record

[Cyswllt i'r cyhoeddiad / Link to publication](#)

*Dyfyniad o'r fersiwn a gyhoeddwyd / Citation for published version (APA):*

Bowden, D., Ward, J., Middleburgh, S., de Moraes Shubeita, S., Zapata-Solvas, E., Lapauw, T., Vleugels, J., Lambrinou, K., Lee, B., Preuss, M., & Frankel, P. (2020). The Stability of Irradiation-Induced Defects in Zr<sub>3</sub>AlC<sub>2</sub>, Nb<sub>4</sub>AlC<sub>3</sub> and (Zr<sub>0.5</sub>,Ti<sub>0.5</sub>)<sub>3</sub>AlC<sub>2</sub> MAX Phase-Based Ceramics. *Acta Materialia*, 183, 24-35. <https://doi.org/10.1016/j.actamat.2019.10.049>

### Hawliau Cyffredinol / General rights

Copyright and moral rights for the publications made accessible in the public portal are retained by the authors and/or other copyright owners and it is a condition of accessing publications that users recognise and abide by the legal requirements associated with these rights.

- Users may download and print one copy of any publication from the public portal for the purpose of private study or research.
- You may not further distribute the material or use it for any profit-making activity or commercial gain
- You may freely distribute the URL identifying the publication in the public portal ?

### Take down policy

If you believe that this document breaches copyright please contact us providing details, and we will remove access to the work immediately and investigate your claim.



Full length article

# The stability of irradiation-induced defects in $Zr_3AlC_2$ , $Nb_4AlC_3$ and $(Zr_{0.5},Ti_{0.5})_3AlC_2$ MAX phase-based ceramics

D. Bowden<sup>a,\*</sup>, J. Ward<sup>a,b</sup>, S. Middleburgh<sup>c</sup>, S. de Moraes Shubeita<sup>d</sup>, E. Zapata-Solvas<sup>e</sup>, T. Lapauw<sup>f</sup>, J. Vleugels<sup>f</sup>, K. Lambrinou<sup>g,h</sup>, W.E. Lee<sup>e</sup>, M. Preuss<sup>a</sup>, P. Frankel<sup>a</sup>

<sup>a</sup>The University of Manchester, School of Materials, Oxford Road, Manchester M13 9PL, United Kingdom

<sup>b</sup>Rolls-Royce plc, Derby, Derbyshire DE24 8BJ, United Kingdom

<sup>c</sup>Nuclear Futures: Materials, Bangor University, Bangor, Gwynedd LL57 2DG, United Kingdom

<sup>d</sup>The University of Manchester, Dalton Cumbrian Facility, Moor Row, CA24 3HA, United Kingdom

<sup>e</sup>Centre for Nuclear Engineering (CNE) & Department of Materials, Imperial College London, London, United Kingdom

<sup>f</sup>KU Leuven, Department of Materials Engineering, Kasteelpark Arenberg 44, Leuven 3001, Belgium

<sup>g</sup>SCK CEN, Boeretang 200, Mol 2400, Belgium

<sup>h</sup>School of Computing and Engineering, University of Huddersfield, Huddersfield, HD1 3DH, United Kingdom



## ARTICLE INFO

## Article history:

Received 26 June 2019

Revised 5 October 2019

Accepted 25 October 2019

Available online 7 November 2019

## Keywords:

Irradiation effect

Ceramics

Density functional theory (DFT)

x-ray diffraction (XRD)

Lattice strains

## ABSTRACT

This work is a first assessment of the radiation tolerance of the nanolayered ternary carbides (MAX phases),  $Zr_3AlC_2$ ,  $Nb_4AlC_3$  and  $(Zr_{0.5},Ti_{0.5})_3AlC_2$ , using proton irradiation followed by post-irradiation examination based primarily on x-ray diffraction analysis. These specific MAX phase compounds are being evaluated as candidate coating materials for fuel cladding applications in advanced nuclear reactor systems. The aim of using a MAX phase coating is to protect the substrate fuel cladding material from corrosion damage during its exposure to the primary coolant. Proton irradiation was used in this study as a surrogate for neutron irradiation in order to introduce radiation damage into these ceramics at reactor-relevant temperatures. The post-irradiation examination of these materials revealed that the Zr-based 312-MAX phases,  $Zr_3AlC_2$  and  $(Zr_{0.5},Ti_{0.5})_3AlC_2$  have a superior ability for defect-recovery above 400 °C, whilst the  $Nb_4AlC_3$  does not demonstrate any appreciable defect recovery below 600 °C. Density functional theory calculations have demonstrated that the structural differences between the 312 and 413-MAX phase structures govern the variation of the irradiation tolerance of these materials.

© 2019 Acta Materialia Inc. Published by Elsevier Ltd.

This is an open access article under the CC BY license. (<http://creativecommons.org/licenses/by/4.0/>)

## 1. Introduction

MAX phase compounds have been considered promising candidate materials for use in accident tolerant fuel (ATF) claddings in 3rd generation (Gen-III) light-water reactors (LWRs) and future (Gen-IV) fission plants [1,2]. This is due to a unique combination of metallic and ceramic properties, such as ductility, thermal shock resistance and machinability, usually exhibited by metals, alongside high stiffness, resistance to high-temperatures and corrosion resistance attributed to ceramics [3,4]. MAX phase compounds have also been reported to exhibit a good ability to annihilate radiation-induced defects at elevated temperatures [5–7]. The MAX phases are nanolayered ternary carbides or nitrides with the stoichiometry  $M_{n+1}AX_n$ , where  $n = 1, 2, \text{ or } 3$ , M is an early transition

metal, A is an element predominantly from group 13 or 14, and X is either carbon or nitrogen [3]. X atoms occupy octahedral sites between the M layers, within a hexagonal unit cell of space-group  $P6_3/mmc$ . Supplementary Fig. S1 demonstrates the typical arrangement of the unit cell in 312 and 413-MAX phases. Strong covalent bonds exist between ‘ceramic’ M-X atoms, whilst weaker covalent bonding exists between M-A atoms and the A-layers are bonded metallicity [3].

Most Gen-IV fission reactors are designed to operate at higher temperatures (in the 500 – 800°C range), higher irradiation fluences (between 150 and 200 dpa) [8,9], using a range of inherently aggressive primary coolants (e.g. heavy liquid metals, molten salts) as compared to Gen-III LWR systems [8]. Pressurised water reactor (PWR) and boiling water reactor (BWR) fuel cladding materials witness a typical radiation damage of 2–5 displacements per atom (dpa) per year [9]. Such neutron fluences typically introduce appreciable microstructural damage into the irradiated materials,

\* Corresponding author.

E-mail address: [david.bowden@ukaea.uk](mailto:david.bowden@ukaea.uk) (D. Bowden).

causing a degradation of mechanical properties, such as irradiation-induced embrittlement, hardening and creep [9,10].

New MAX phase compounds, with an M element of Zr, Nb and/or Ti, have been fabricated as potential fuel cladding coating materials either for ATF applications (LWRs), or for next-generation nuclear systems with corrosive primary coolants (e.g. Gen-IV lead-cooled fast reactors, LFRs) [11–15]. Zr-based MAX phases are of particular interest due to the small neutron cross-section of Zr and the promising performance of ZrC-based ceramics in nuclear environments [16,17]. Whilst the neutron cross-section of Nb is larger than Zr, the ability to synthesise (Nb,Zr)-based MAX phases and their favorable refractory metal properties justifies the interest in Nb-based compositions.

This study seeks an initial assessment of the radiation response of  $Zr_3AlC_2$ ,  $Nb_4AlC_3$  and  $(Zr_{0.5},Ti_{0.5})_3AlC_2$  MAX phase-based ceramics at irradiation test temperatures targeting nominal operation conditions in Gen-III LWRs or Gen-IV nuclear systems, such as the LFR concept. Previous studies into the irradiation-response of MAX phase-based ceramics have focussed almost exclusively on Ti-based compounds [5,7,18–26]. Dual Zr/Ti MAX phase solid solutions are attractive due to the reduction of the material neutron cross-section through the partial replacement of Ti by Zr [15]. Proton ( $H^+$ ) irradiation of these ceramics has been carried out to two specific damage levels allowing an assessment of the lattice response of each material to these irradiations. In the case of  $Zr_3AlC_2$ , an additional high-damage level has been investigated within this study.  $H^+$  irradiation is used as a surrogate for neutron irradiation, primarily because protons allow irradiation damage to be rapidly generated within a material, without significant post-irradiation material activation. It is accepted that  $H^+$  irradiation produces damage structures comparable to neutron irradiation, but caution must be applied when comparing both types of irradiation [27].  $H^+$  suffers a reduced penetration depth, so the depth of the region analysed must be carefully controlled to ensure consistent levels of damage are being assessed. Additionally,  $H^+$  irradiation will produce a wider energy range of primary knock-on atoms (PKA's) compared to neutron irradiation [28]. This results in smaller defect clusters within  $H^+$  irradiated materials.

In this study, density functional theory (DFT) has been employed to provide insight into the likely radiation-induced defect mechanisms occurring in the  $Zr_3AlC_2$  and  $Nb_4AlC_3$  MAX phases. Alongside the irradiation study, baseline characterisation of the microstructures for both compositions is presented establishing an understanding of the importance of phase purity. Part of the assessment of the suitability of these materials for fuel cladding applications involves investigating their capability to anneal irradiation damage and the MAX phase stability at elevated temperatures. Therefore, the results of a combined in-situ heating and x-ray diffraction (XRD) study are also presented here, so as to investigate the material recovery behaviour.

## 2. Experimental methods

### 2.1. Materials synthesis

The laboratory-grade MAX-phase based ceramics  $Zr_3AlC_2$  and  $Nb_4AlC_3$  were supplied by KU Leuven, Belgium, whilst  $(Zr_{0.5},Ti_{0.5})_3AlC_2$  was supplied by Imperial College London, UK. All samples were supplied in the form of circular billets of 2 mm thickness and 40 mm diameter, produced by the reactive hot-pressing method. This method involves mixing pure-element powders, followed by hot pressing at: 1500 °C for  $Zr_3AlC_2$  or 1700 °C for  $Nb_4AlC_3$  for 30 min at 20 MPa pressure, and 1450 °C for  $(Zr_{0.5},Ti_{0.5})_3AlC_2$  for 60 min at 30 MPa pressure. Greater detail of the fabrication methodologies can be found elsewhere [12,13,15]. The billets were then cut into matchsticks, suitable for  $H^+$  irradi-

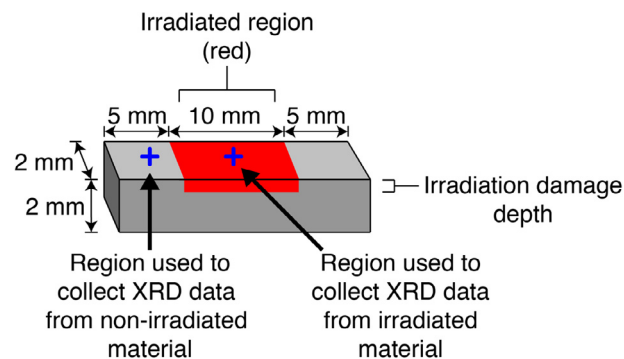


**Fig. 1.** Schematic representation of an irradiated matchstick sample, indicating the different areas used for XRD data acquisition (blue crosses). (For interpretation of the references to colour in this figure legend, the reader is referred to the web version of this article.)

ation. These matchsticks were typically  $2 \times 2 \times 20$  mm in size and cut using electro-discharge machining (EDM), as shown in Fig. 1. The matchsticks were polished to a mirror finish using colloidal silica suspension. The pre-irradiation characterisation of the prepared matchsticks is described in the following sections.

### 2.2. Microstructural characterisation

Electron backscatter diffraction (EBSD) and energy-dispersive x-ray spectroscopy (EDS) were used to characterise the as-received (AR) materials using an FEI Quanta 250 field emission gun (FEG)-scanning electron microscope (SEM) for  $Zr_3AlC_2$  and a Zeiss Sigma FEG-SEM for  $Nb_4AlC_3$  and  $(Zr_{0.5},Ti_{0.5})_3AlC_2$ . The Quanta 250 was fitted with an Oxford Instruments NordlysNano EBSD detector and Oxford Instruments X-Max<sup>N</sup> 80 mm<sup>2</sup> EDS detector. The Zeiss Sigma uses an Oxford Instruments NordlysNano EBSD detector and Oxford Instruments X-Max<sup>N</sup> 150 EDS detector. Secondary electron (SE) images were captured using an accelerating voltage of 20 kV. EBSD maps were captured using a 200 nm step-size and 20 kV accelerating voltage with EDS maps collected in parallel.

Porosity was measured by image analysis on SEM micrographs obtained from each sample of  $Zr_3AlC_2$ ,  $Nb_4AlC_3$  and  $(Zr_{0.5},Ti_{0.5})_3AlC_2$  in the AR condition. Porosity analysis was performed on image areas of at least  $560 \times 370$   $\mu\text{m}$ . The SE images were thresholded using Fiji v1.51 [29], leaving only pores visible, allowing the area fraction of porosity to be calculated. Features classified as pores were identified by the characteristic electron charging of the pore edge, which results in an increase in SE image brightness around such features. Pores could also be confirmed from EBSD data, with pores showing zero band-contrast.

Post-irradiation microscopy was carried out using a Zeiss Sigma FEG-SEM operating at 20 kV. SE images were collected from both irradiated and non-irradiated regions of the sample surface, as illustrated in Fig. 1.

### 2.3. Density functional theory

In order to better understand the likely mechanisms of radiation damage in these materials, intrinsic defect calculations were carried out using DFT to determine the most favourable lattice defects in  $Zr_3AlC_2$  and  $Nb_4AlC_3$ . Vacancies, anti-site defects and interstitials were considered. Vacancies and anti-sites were considered as isolated defects on each symmetrically distinct lattice site. A total of eight interstitial sites were considered for each element within the 312-MAX phase structure and ten sites within the 413-MAX phase structure. The typical crystal structures for 312 and 413-MAX phases are shown in Supplementary Fig. S1.

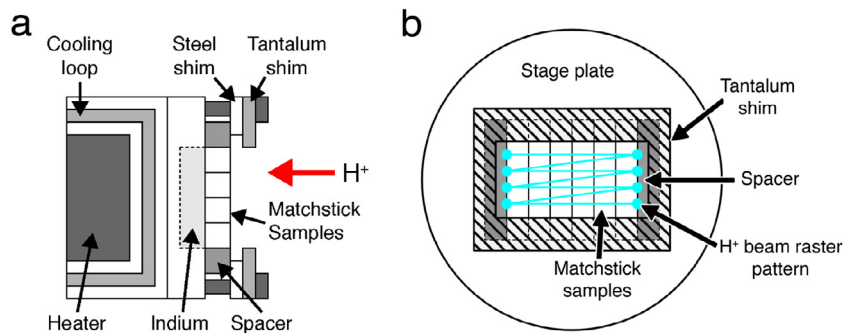


**Fig. 2.** Schematic of the experimental setup used for proton irradiation: (a) lateral view of the heated stage assembly; (b) view normal to the sample surface, demonstrating the  $H^+$  ion beam raster pattern used to homogeneously irradiate the sample surface.

Atomistic simulations were carried out using the DFT Vienna Ab-initio Simulation Package (VASP) [30,31], using static calculations at the reaction enthalpy (0 K). Previously calculated nudged elastic band (NEB) migration energy barriers for  $Ti_3SiC_2$  and  $Ti_3AlC_2$  MAX phase structures [32] were used to inform the study carried out here. A  $3 \times 3 \times 3$  supercell of the  $Nb_4AlC_3$  and  $Zr_3AlC_2$  MAX phase structures (both with  $P6_3/mmc$  symmetry in the Hermann-Mauguin notation) were used for all calculations containing 144 lattice sites (72 Nb, 18 Al and 54 C) and 108 lattice sites (54 Zr, 18 Al and 36 C), for the  $Nb_4AlC_3$  and  $Zr_3AlC_2$  MAX phases, respectively. A cut-off energy of 450 eV was used for all calculations which were performed under constant pressure, allowing the size and shape of the supercell to vary with the atomic positions. The self-consistent field convergence criterion was set at  $1 \times 10^{-5}$  eV and the geometry optimization convergence criterion was set at  $1 \times 10^{-4}$  eV. Projector augmented wave potentials [33] were chosen from the VASP library, which utilized the general gradient approximation exchange correlation, as determined by Perdew, Burke and Ernzerhof (GGA-PBE [34]). A  $4 \times 4 \times 4$   $k$ -point grid was used for all calculations and a Methfessel-Paxton smearing method was used with a smearing width of 0.2 eV.

#### 2.4. Proton irradiation and post-irradiation examination by XRD

Proton ( $H^+$ ) irradiation was carried out at the Dalton Cumbrian Facility (DCF) of the University of Manchester, Cumbria, UK [35]. Fig. 2a outlines a cross-sectional view of the sample and stage arrangement used in this study. The  $Zr_3AlC_2$ ,  $Nb_4AlC_3$  and  $(Zr_{0.5},Ti_{0.5})_3AlC_2$  matchstick samples were aligned across an indium-well and secured using both steel and tantalum shims. A heater and a cooling loop below the indium well ensured thermal control during the irradiation experiments. A window cut into the shims allowed the  $H^+$  beam to be rastered across the sample surface, as illustrated in Fig. 2b.

Irradiations were carried out using 2 MeV  $H^+$  with a flux of  $2.5 \times 10^{13} H^+ cm^{-2} \cdot s^{-1}$ . Fluences of both  $1.8 \times 10^{17} H^+ cm^{-2}$  and  $1.8 \times 10^{18} H^+ cm^{-2}$  were used to produce samples of low (approximately 0.01 dpa) and moderate (approximately 0.1 dpa) doses, respectively, within the plateau region of proton-induced damage. The dose rate in the plateau region of interest (defined below) at both low and moderate dose level, was approximately  $1.3 \times 10^{-6} dpa \cdot s^{-1}$ . The  $Zr_3AlC_2$ -based ceramic was additionally irradiated at a flux of  $8.9 \times 10^{13} H^+ cm^{-2} \cdot s^{-1}$  and a fluence of  $1.35 \times 10^{19} H^+ cm^{-2}$ , to a high dose of approximately 1 dpa. This corresponds to a dose rate of  $5.3 \times 10^{-6} dpa \cdot s^{-1}$  in the plateau region. A  $10 \times 2$  mm area in the centre of each matchstick sample was irradiated (Fig. 1). Two irradiation temperatures of 350 °C and 575 °C were selected, which allows thermal conditions similar to both Gen-III and Gen-IV reactors, respectively, to be simulated. Therefore, 14 samples (i.e.,  $6 \times Zr_3AlC_2$ ,  $4 \times Nb_4AlC_3$ ,

$4 \times (Zr_{0.5},Ti_{0.5})_3AlC_2$ ) were irradiated at each dose and temperature combination described above. The maximum permissible temperature variation at the sample surface was  $\pm 10$  °C, measured using infrared detectors, calibrated using a thermocouple reading prior to irradiation. The use of line-profile measurements ensured homogeneity of the temperature distribution across the sample surface.

Dose profiles for  $Zr_3AlC_2$ ,  $Nb_4AlC_3$  and  $(Zr_{0.5},Ti_{0.5})_3AlC_2$  were simulated using the Stopping Range of Ions in Matter (SRIM) 2013 software package [36] (Fig. 3). The quick Kinchin-Pease calculation was applied to simulate the collision of 100,000  $H^+$  ions into the sample surface. Standard displacement threshold values were used for the SRIM calculations, i.e. 25 eV for Zr, Nb, Ti and Al and 28 eV for C. For 2 MeV  $H^+$ , the Bragg peak (maximum damage) in  $Zr_3AlC_2$  (theoretical density of  $5.62 g \cdot cm^{-3}$ ) occurs 30  $\mu m$  below the irradiated face (Fig. 3a).  $Nb_4AlC_3$  has a theoretical density of  $7.04 g \cdot cm^{-3}$ , therefore, the proton stopping ranges are shorter; i.e. the Bragg peak occurs at 23.5  $\mu m$  below the irradiated specimen surface (Fig. 3b).  $(Zr_{0.5},Ti_{0.5})_3AlC_2$  has a theoretical density of  $4.92 g \cdot cm^{-3}$  and the Bragg peak occurs at 29.6  $\mu m$  below the irradiated specimen surface (Fig. 3c).

Post-irradiation analysis of the matchsticks was carried out using XRD. Two sites were selected per sample: one located 2.5 mm from the sample edge in the non-irradiated region, and one in the middle of the 10 mm-long irradiated region in the centre of the matchstick. Both positions were situated halfway across the 2-mm matchstick width. The schematic in Fig. 1 illustrates this arrangement. By collecting XRD data from these sites, it was possible to monitor the radiation-induced lattice changes in each specimen.

It was important to calculate the linear absorption coefficient (LAC) of x-rays generated from a Co source ( $\lambda = 1.79 \text{ \AA}$ ), penetrating normal to the sample irradiated surface, in order to control the depth from which x-ray data is generated. The variation in the generated x-ray signal intensity as a function of the penetration depth is plotted in Fig. 3. This approach allows the accumulated damage at the plateau region of the SRIM profile to be determined. The plateau region provides a relatively consistent level of  $H^+$  dose across a larger region of irradiated material.

To be more precise, it was decided that the depth from which 70% of the x-ray signal was generated should define the plateau damage, since laboratory x-ray signals below 30% intensity are obscured by noise [37]. It was determined that the plateau depth in  $Zr_3AlC_2$  was approximately 14  $\mu m$  (Fig. 3a), in  $Nb_4AlC_3$  it was 10  $\mu m$  (Fig. 3b) and in  $(Zr_{0.5},Ti_{0.5})_3AlC_2$  it was 14.5  $\mu m$  (Fig. 3c). The irradiations were designed in such a manner that the targeted damage levels were achieved within the sample plateau region. The dose achieved per sample varied depending on material stoichiometry and density and is summarised in Table 1.

A Bruker D8-Discover with a Co source ( $\lambda = 1.79 \text{ \AA}$ ) was used in the theta-theta setup to perform the XRD analysis. A Göbel

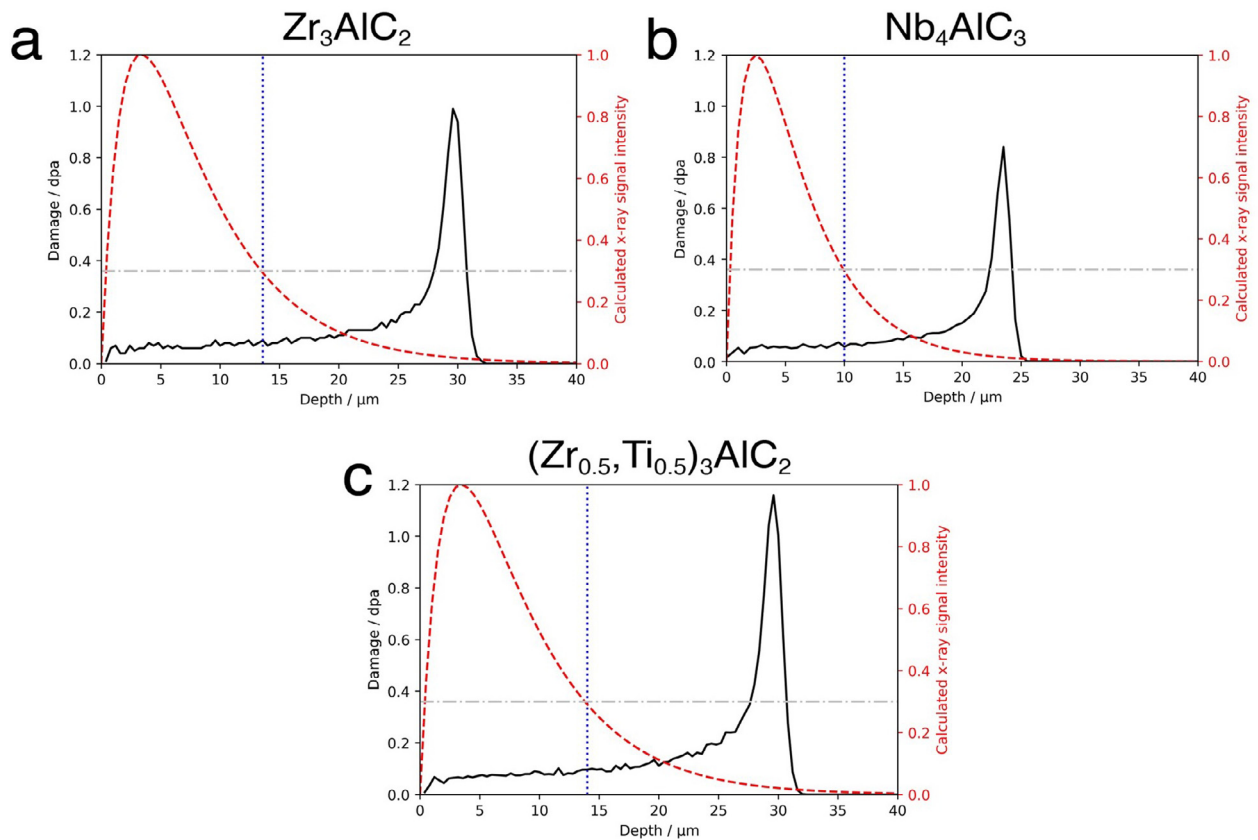


**Fig. 3.** SRIM profiles for: (a)  $Zr_3AlC_2$ , (b)  $Nb_4AlC_3$  and (c)  $(Zr_{0.5},Ti_{0.5})_3AlC_2$ , calculated for 2 MeV  $H^+$  ions at a fluence of  $1.8 \times 10^{18}$  protons  $cm^{-2}$  together with the normalised x-ray signal intensity generated as a function of the proton ( $H^+$ ) penetration depth. The depth of detectable x-ray signal at 30% signal intensity (shown by dash-dot horizontal grey lines) or lower is indicated by dotted vertical blue lines. (For interpretation of the references to colour in this figure legend, the reader is referred to the web version of this article.)

mirror was used to produce a parallel, monochromatic beam on the samples. Vertical slits of 0.1 mm across ensured that the beam would not spill over the width of the matchstick at shallower angles, whilst a horizontal masque exposed only 5 mm of the matchstick length at each point, ensuring that the analysed regions were either fully irradiated or non-irradiated. A collection  $2\theta$  range of  $30 - 140^\circ$  was used per scan, with a  $0.02^\circ$  step size, counting for  $3.8 \text{ s}\cdot\text{step}^{-1}$ .

XRD data were analysed using TOPAS v5 [38], whereby full Rietveld structural fits were performed on each dataset. Typical goodness of fit (GOF) values ranged between 2.5 and 3.5, although for the  $Nb_4AlC_3$ -based ceramics that were irradiated to moderate-damage, GOF values increased to 6.8. This is attributed to a large variation in peak intensities that were difficult to fit perfectly with texture correction routines. However, peak positions were inspected manually to ensure that peak centres were fitted accurately since these governed the measured lattice parameters. The percentage changes in lattice parameters, calculated from the Rietveld refinements, could then be compared between the irradiated and non-irradiated regions of the specimens.

### 2.5. Variable temperature XRD study

$Zr_3AlC_2$  and  $Nb_4AlC_3$  in both the non-irradiated, as-received (AR) and low-damage  $350^\circ\text{C}$  irradiated conditions were studied using an in-situ variable temperature (VT) XRD set up. A Bruker-D8 Advance operating with a Cu source ( $\lambda = 1.54 \text{ \AA}$ ) was used to collect the data, whilst the samples were enclosed in a Material Research Institute (MRI) environmental VT stage. A nitrogen purge minimised sample oxidation during testing. Once again, the match-

**Table 1**

Actual irradiation damage achieved in the plateau region of each sample, given in displacements per atom (dpa). Only  $Zr_3AlC_2$  was irradiated to the high damage dose of  $\sim 1$  dpa.

Composition	Damage dose (dpa)		
	Low	Moderate	High
$Zr_3AlC_2$	0.009	0.091	0.794
$Nb_4AlC_3$	0.009	0.085	–
$(Zr_{0.5},Ti_{0.5})_3AlC_2$	0.010	0.099	–

stick centres were used to collect data from the fully irradiated region (Fig. 1). AR materials were supplied as  $10 \times 10 \times 2 \text{ mm}$  cuboids with a beam size of  $2 \times 0.6 \text{ mm}$  positioned at the sample centre.

XRD patterns were collected at specific points along a temperature profile. These were: room temperature (RT;  $25^\circ\text{C}$ ),  $200^\circ\text{C}$ ,  $300^\circ\text{C}$ ,  $350^\circ\text{C}$ ,  $400^\circ\text{C}$ ,  $450^\circ\text{C}$ ,  $500^\circ\text{C}$ ,  $550^\circ\text{C}$  and  $600^\circ\text{C}$ , before finally cooling down to RT, where the final XRD pattern was collected. The temperature profile is shown in Supplementary Fig. S2. The heating/cooling rate used was  $10^\circ\text{C}\cdot\text{min}^{-1}$ . Patterns were collected across a  $2\theta$  range of  $30$  to  $75^\circ$ , with a step size of  $0.03^\circ$  and a counting time of  $5 \text{ s}\cdot\text{step}^{-1}$ , equating to a dwell time of approximately 2 h. Inspection of peak-shifts during a trial experiment of AR  $Zr_3AlC_2$  gave confidence that the microstructure rapidly reaches steady-state conditions once the scan commenced during the sample dwell at elevated temperatures. Once again, data analysis was carried out using TOPAS v5 [38], generating full Rietveld structural fits. The analysis yielded favourable GOF values, ranging between 1.1 and 2.6 for all datasets. At each temperature step, changes in

**Table 2**

Summary of the phase fractions of  $Zr_3AlC_2$ ,  $Nb_4AlC_3$  and  $(Zr_{0.5},Ti_{0.5})_3AlC_2$  MAX phase-based ceramics determined from XRD data. All phase fractions are given in wt.%. Uncertainties shown in parentheses.

	$Zr_3AlC_2$	$(Zr_{0.5},Ti_{0.5})_3AlC_2$	$(Zr_{0.5},Ti_{0.5})_2AlC$	$Nb_4AlC_3$	$(Zr,Ti)C$	$Al_2Zr$	$Ti_3Al$	$Zr_2Al_3$	$Al_3Nb$
$Zr_3AlC_2$	44(4)	–	–	–	12(1)	–	–	44(3)	–
$Nb_4AlC_3$	–	–	–	93(2)	–	–	–	–	7(2)
$(Zr_{0.5},Ti_{0.5})_3AlC_2$	–	59(15)	18(4)	–	17(11)	2(2)	3(1)	–	–

the  $a$  and  $c$  lattice parameters were calculated from the Rietveld analysis of the XRD data.

### 3. Results and discussion

#### 3.1. Baseline characterisation of AR $Zr_3AlC_2$ , $Nb_4AlC_3$ and $(Zr_{0.5},Ti_{0.5})_3AlC_2$

XRD was used to establish the phase purity of the AR samples of  $Zr_3AlC_2$ ,  $Nb_4AlC_3$  and  $(Zr_{0.5},Ti_{0.5})_3AlC_2$ . Typical XRD patterns for these ceramics are shown in Supplementary Fig. S3 whilst the phase fraction results (measured in wt.%) are presented in Table 2. The  $Zr_3AlC_2$  billet had a low MAX phase content with a fraction of 44(4) wt.%. Within the same material, the intermetallic compound  $Zr_2Al_3$  accounted for 44(3) wt.%, whilst the ZrC carbide accounted for 12(1) wt.%. The  $(Zr_{0.5},Ti_{0.5})_3AlC_2$  billet was also characterised by a moderate MAX phase content, consisting of 59(15) wt.% 312-MAX phase  $(Zr_{0.5},Ti_{0.5})_3AlC_2$ , 18(4) wt.% 211-MAX phase  $(Zr_{0.5},Ti_{0.5})_2AlC$  and 17(11) wt.%  $(Zr,Ti)C$  carbide. In addition, small amounts of intermetallic phases were detected, i.e. 2(2) wt.% of  $Al_2Zr$  and 3(1) wt.% of  $Ti_3Al$ . Contrary to this, the  $Nb_4AlC_3$  billet had a MAX phase purity of 93(2) wt.% and 7(2) wt.%  $Al_3Nb$  intermetallic. These findings are in agreement with previous works reporting the difficulty in achieving a high phase purity in Zr-based MAX phase ceramics [12,39]. This is opposed to Nb-based MAX phases where phase-pure samples are more readily synthesised.

The EBSD phase map of  $Zr_3AlC_2$  demonstrates its microstructural heterogeneity (Fig. 4a). MAX phase grains are easily distinguished by their lath-like habit when compared to the equiaxed secondary phases ZrC and  $Zr_2Al_3$ . It is known that the MAX phases grow more rapidly along the  $a$ -direction than the  $c$ -direction [40]. In addition, observation of the inverse pole figure (IPF) orientations along the Z direction (i.e. the direction normal to the viewing plane) indicates that MAX phase grains become aligned with the  $\langle 0001 \rangle$  direction, parallel to the compression axis during sintering (Fig. 4b), as previously reported [12]. The lath-like grain morphology of  $Nb_4AlC_3$  is more readily visible (Fig. 4c), where  $Al_3Nb$  occupies dispersed regions between the  $Nb_4AlC_3$  laths. Once again, a slight preference for grain alignment along the  $\langle 0001 \rangle$  direction is observed (Fig. 4d). The microstructures of  $Zr_3AlC_2$  (Fig. 4a) and  $(Zr_{0.5},Ti_{0.5})_3AlC_2$  (Fig. 4e) are similar. Significant microstructural heterogeneity is also observed in  $(Zr_{0.5},Ti_{0.5})_3AlC_2$  where finer  $(Zr,Ti)C$  precipitates cluster between the MAX phase grains (Fig. 4e and f). EBSD mapping was unable to distinguish the  $(Zr_{0.5},Ti_{0.5})_3AlC_2$  and  $(Zr_{0.5},Ti_{0.5})_2AlC$  MAX phase grains, due to the fact that both phases share the  $P6_3/mmc$  space-group and have nearly identical  $a$ -lattice parameters. However, the 37% difference in  $c$ -lattice parameter (i.e. 19.39 Å for  $(Zr_{0.5},Ti_{0.5})_3AlC_2$  and 14.16 Å for  $(Zr_{0.5},Ti_{0.5})_2AlC$ ) should theoretically allow the two phases to be discerned by EBSD, but in this case a combination of the measurement settings and/or the equipment sensitivity prevented this.

The apparent tendency of the  $Zr_3AlC_2$  phase towards decomposition during processing leads to a grain size refinement, which is likely due to the precipitation of the secondary phases in this material. The average  $Zr_3AlC_2$  phase grain size was 1.8(1)  $\mu m$  along the lath-length and 1.0(1)  $\mu m$  along the lath-width. The

greater MAX phase content in the  $(Zr_{0.5},Ti_{0.5})_3AlC_2$  ceramic, promoted the formation of larger grains with 3.1(1)  $\mu m$  along the lath-length and 1.7(1)  $\mu m$  along the lath-width. In comparison, the  $Nb_4AlC_3$  ceramic possessed the largest MAX phase grains with an average lath-length of 5.2(3)  $\mu m$  and a lath-width of 2.6(2)  $\mu m$ .

SE detector images of the AR ceramic microstructures revealed microcracking within the  $Zr_3AlC_2$  laths (Fig. 5a). As the MAX phase laths grow along the  $a$ -direction [40], it is inferred that the cracks develop along the basal planes, normal to the  $c$ -direction.  $Nb_4AlC_3$ , on the other hand, bears some evidence of cracking normal to the  $c$ -direction in the AR condition (Fig. 5d), but not to the same extent as the  $Zr_3AlC_2$ . Cracking within the MAX phase laths of the AR  $(Zr_{0.5},Ti_{0.5})_3AlC_2$  was not observed (Fig. 5g). The possible reasons for the observed cracking in the  $Zr_3AlC_2$  MAX phase grains will be discussed later.

Low-magnification SE images allow the determination of the levels of porosity in the AR MAX phase ceramics. The  $Nb_4AlC_3$  ceramic exhibited a high level of porosity at a fraction of 5.17%.  $Zr_3AlC_2$  had a porosity level of 3.49%, whilst the  $(Zr_{0.5},Ti_{0.5})_3AlC_2$  was the least porous, at a fraction of 0.41%. It is worthwhile to note that surface damage resembling porosity is introduced during sample preparation, particularly by way of grain pull-out during grinding. Fine particles of  $Al_2O_3$ , present from the reactive hot press process, are particularly susceptible to pull-out during grinding. Therefore, the porosity determined here, is expected to be larger than the porosity actually present in the samples after fabrication.

#### 3.2. XRD study of proton-irradiated materials

Proton-irradiated matchsticks from each material were assessed for lattice parameter changes using XRD. It should be noted that since separate XRD signals are produced by specific phases within each material, the changes observed in irradiated MAX phase grains present in the heterogeneous  $Zr_3AlC_2$  and  $(Zr_{0.5},Ti_{0.5})_3AlC_2$  ceramics can be assessed independently, despite the low MAX phase yield in these materials. The lattice  $c$ -parameter was observed to increase from the non-irradiated to the irradiated condition, at both low- and moderate-damage levels and both irradiation temperatures (350 and 575 °C), as shown in Fig. 6a to c.

Usually, the irradiation-induced  $c$ -parameter expansion in MAX phases is accompanied by an  $a$ -parameter contraction [5,7,18,21,24,26,41–43]. Fig. 6b–d shows the changes in  $a$ - and  $c$ -parameters side-by-side. At low damage, the  $a$ -parameter contraction is too small to be reliably observed. However, the lattice parameter changes at moderate and high damage levels ( $\sim 0.1$  dpa and greater) show the effect of  $a$ -parameter contraction due to an anisotropic unit cell distortion more clearly (Fig. 6c and d). Of great interest here is the obvious difference in  $c$ -parameter expansion between the Zr-based 312-MAX phases and the Nb-based 413-MAX phase.

At 350 °C, all samples exhibit high levels of  $c$ -parameter expansion, although in most cases,  $Nb_4AlC_3$  appears to perform marginally better than the Zr-based MAX phases (Fig. 6a to c). However, when irradiated at 575 °C, this behaviour changes, and the Zr-based MAX phases show a greatly reduced  $c$ -parameter

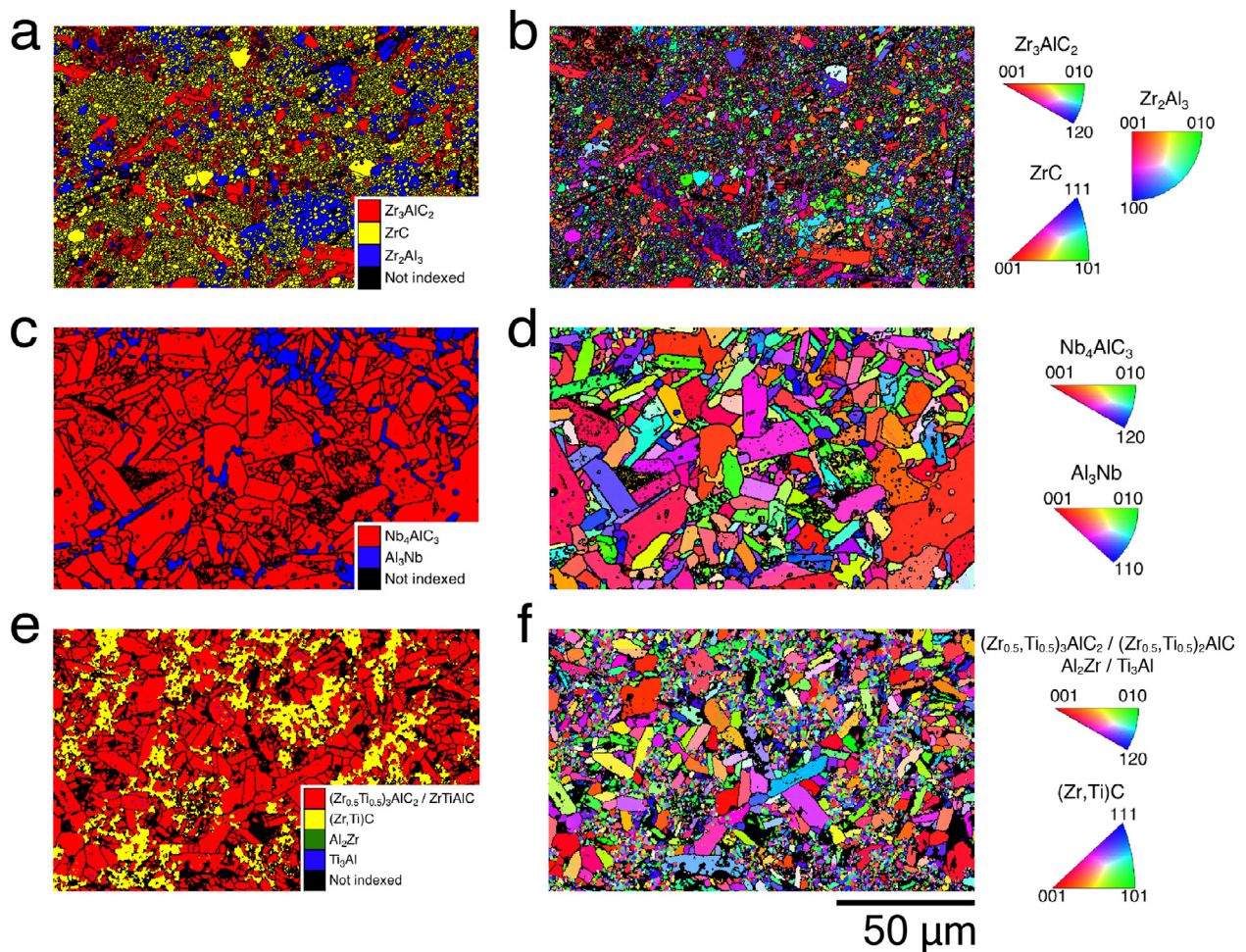


**Fig. 4.** EBSD phase maps (left column) and IPF-Z maps (right column) of typical non-irradiated microstructures in the: (a,b)  $Zr_3AlC_2$ ; (c,d)  $Nb_4AlC_3$  and (e,f)  $(Zr_{0.5}Ti_{0.5})_3AlC_2$  MAX phase-based ceramics. Orientation IPF-Z legends for the major phases are indicated to the right of the IPF-Z maps. Grain and phase boundaries are shown in black.

expansion as compared to  $Nb_4AlC_3$  (Fig. 6a to c). The observed lattice recovery of the MAX phases at high temperatures has been reported in previous studies, such as that by Tallman et al. [18], whereby lattice recovery was observed in Ti-based MAX phases at 695 °C. At the high-damage level of 1 dpa at 350 °C,  $Zr_3AlC_2$  demonstrates a significant *c*-parameter expansion of 2.41%, which is reduced to 0.21% at 575 °C (Fig. 6a and d).

These findings suggest that the Zr-based 312-MAX phases  $Zr_3AlC_2$  and  $(Zr_{0.5}Ti_{0.5})_3AlC_2$  have a superior capability for defect-recovery in the 350–575 °C temperature range as compared to  $Nb_4AlC_3$ . It is postulated that  $Zr_3AlC_2$  and  $(Zr_{0.5}Ti_{0.5})_3AlC_2$  exhibit such promising high-temperature irradiation tolerance when compared to  $Nb_4AlC_3$ , partly due to the microstructural differences between these ceramics, and partly due to the increased refractory properties of  $Nb_4AlC_3$ . Both  $Zr_3AlC_2$  and  $(Zr_{0.5}Ti_{0.5})_3AlC_2$  have finer grain sizes and higher amounts of secondary phases (Fig. 4a and e) as compared to  $Nb_4AlC_3$  (Fig. 4c), providing a greater number of sites that can act as defect sinks, such as grain boundaries [44]. Moreover, the 413  $Nb_4AlC_3$  MAX phase is known for its outstanding high-temperature stability, retaining its flexural strength up to 1400 °C [45]. Therefore, it is expected that its potential for dynamic recovery of radiation-induced defects will be shifted to higher temperatures as compared to the 312 Zr-based MAX phases  $Zr_3AlC_2$  and  $(Zr_{0.5}Ti_{0.5})_3AlC_2$ . This work includes a DFT study on how differences in the atomic structural configuration of these MAX phases relates to their radiation response.

### 3.3. SEM study of proton-irradiated materials

SE detector imaging was used to assess the integrity of these ceramics after undergoing such an irradiation-induced distortion. SE images of the sample surfaces in both the AR and moderate-damage states, after  $H^+$  irradiation at 350 and 575 °C are shown in Fig. 5. In the AR condition,  $Zr_3AlC_2$  shows clear lath-wise cracking of the MAX phase grains (Fig. 5a). After irradiation at 350 °C, the lath-wise cracks appear to be reduced in number, likely because of the expansion of the MAX phase grains in the *c*-direction, which results in the partial closure of these cracks (Fig. 5b). Cracking was not readily observed in  $Zr_3AlC_2$  irradiated at 575 °C (Fig. 5c).  $Nb_4AlC_3$  exhibited lath-wise cracking in the AR condition (Fig. 5d), which developed into more severe intergranular cracking after moderate-damage irradiation at 350 °C (Fig. 5e). Cracking of  $Nb_4AlC_3$  was not clearly observed after irradiation at 575 °C (Fig. 5f).  $(Zr_{0.5}Ti_{0.5})_3AlC_2$  did not exhibit significant cracking in the AR region of the matchstick (Fig. 5g), but intergranular cracking was observed after moderate damage irradiation at 350 °C (Fig. 5h). Cracking was not readily observed in the  $(Zr_{0.5}Ti_{0.5})_3AlC_2$  irradiated to a moderate-damage at 575 °C (Fig. 5i). The relatively reduced crack severity of  $(Zr_{0.5}Ti_{0.5})_3AlC_2$  irradiated at 350 °C as compared to the irradiated  $Nb_4AlC_3$ , may be partly attributed to the finer-grained, heterogeneous microstructure of the former, which provides a greater number of sites for stress-relief within the microstructure, limiting the extent of any crack growth. The greater stiffness of  $Nb_4AlC_3$  relative to the Zr-based MAX phase

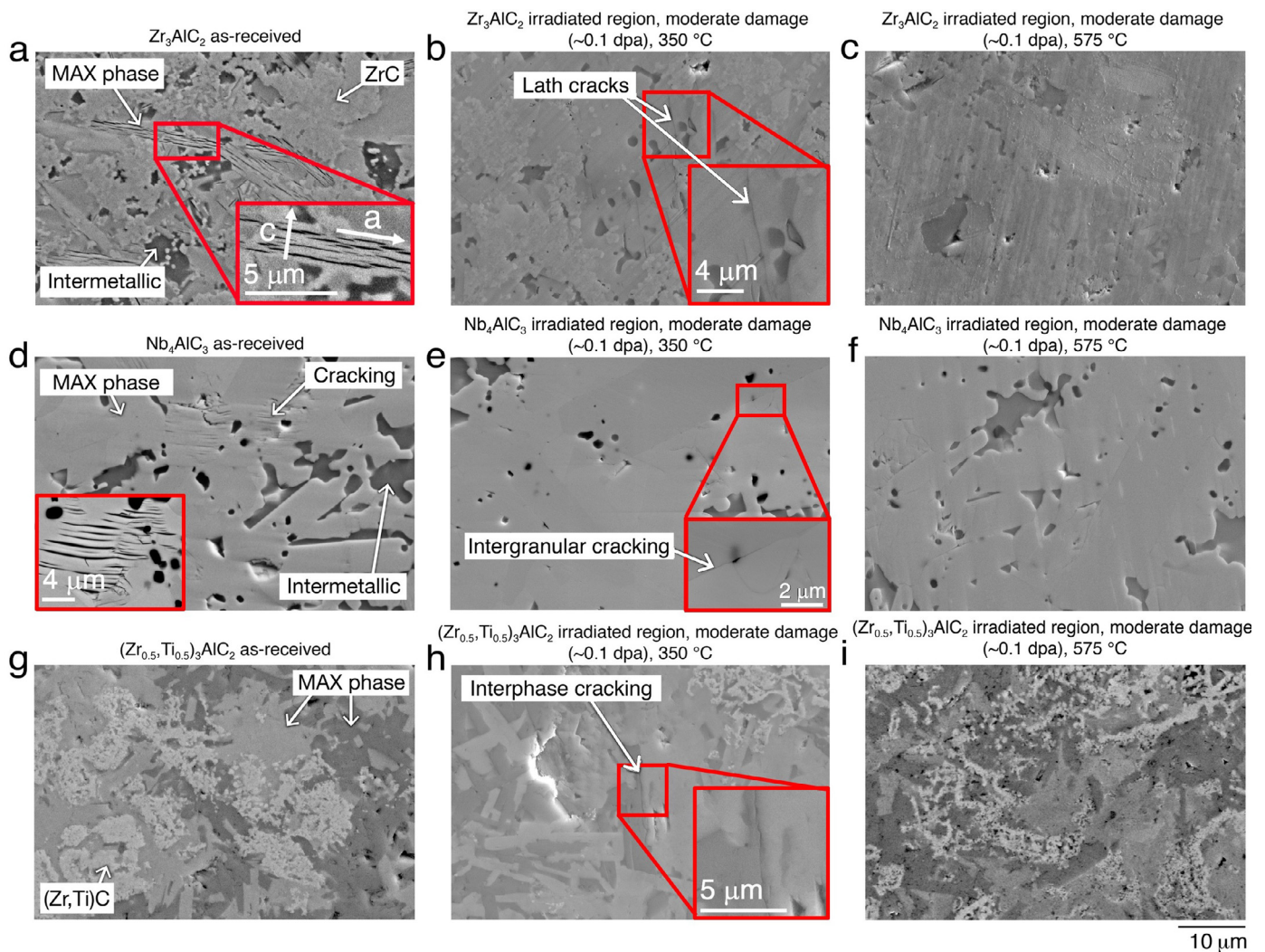


**Fig. 5.** SE-detector images of the irradiated matchsticks in the as-received (AR) and moderate irradiation damage level ( $\sim 0.1$  dpa) states. (a) AR  $Zr_3AlC_2$  showing interlath cracks (the inset shows crack formation between basal planes); (b)  $Zr_3AlC_2$  irradiated at 350  $^{\circ}C$ , showing a reduced number of interlath cracks (inset); (c)  $Zr_3AlC_2$  irradiated at 575  $^{\circ}C$ ; (d) AR  $Nb_4AlC_3$  showing fine interlath cracks (inset image shows cracking at a different region); (e)  $Nb_4AlC_3$  irradiated at 350  $^{\circ}C$ , showing intergranular cracks between MAX phase grains (inset); (f)  $Nb_4AlC_3$  irradiated at 575  $^{\circ}C$ ; (g) AR  $(Zr_{0.5}, Ti_{0.5})_3AlC_2$ ; (h)  $(Zr_{0.5}, Ti_{0.5})_3AlC_2$  irradiated at 350  $^{\circ}C$ , showing regions of interphase cracking (inset); (i)  $(Zr_{0.5}, Ti_{0.5})_3AlC_2$  irradiated at 575  $^{\circ}C$ , no cracks observed.

compounds [45] would also encourage increased levels of crack formation.

### 3.4. DFT calculations of radiation-induced defects

#### 3.4.1. $Nb_4AlC_3$

Following the findings of the XRD study on the proton-irradiated MAX phase ceramics, DFT simulations were performed to understand the effect of the MAX phase crystal structure on the material's capability for defect-recovery. The original non-irradiated, pristine  $Nb_4AlC_3$  lattice is shown in Supplementary Fig. S4e. Both Nb and C have two symmetrically distinct sites within the  $Nb_4AlC_3$  structure (M-1 and M-2 for Nb; C-1 and C-2 for C; see Supplementary Fig. S1b). It was found that the Nb vacancy is most stable, by a margin of 0.78 eV, within the M-1 layer close to the A-layer. This behaviour has been previously observed in MAX phases with partly different stoichiometries, such as  $Ti_3AlC_2$  and  $Ti_3SiC_2$  [32]. Conversely, the C vacancy is most stable, by a margin of 0.82 eV, in the layer furthest from the A-layer (C-2) within the  $Nb_4AlC_3$  lattice.

Nb, Al and C interstitials were most stable in the A-layer. The C interstitial preferentially resides in the  $(0, 0, \frac{1}{4})$  interstitial site,

which is similar to the preferential C interstitial in  $Ti_3SiC_2$  [32]. In this position, the C atom is coordinated in the z-direction by two Nb atoms (above and below) and by three Al atoms within the basal plane. The C-Al distance is 1.98  $\text{\AA}$  and the C-Nb distance is 2.13  $\text{\AA}$  (both have similar bond lengths in their respective binary carbides). The second most favourable interstitial site for C lies between the A and M-1 layer and is 0.93 eV less favourable than the  $(0, 0, \frac{1}{4})$  site. Other considered interstitial sites have energies greater than 2 eV less favourable than the most stable C interstitial site. C Frenkel pairs (Supplementary Fig. S4f) will have difficulty recombining given the multiple atomic layers between the preferred interstitial sites and the preferred vacancy sites (a minimum of 6.0  $\text{\AA}$  away). The calculated C Frenkel formation energy is 1.48 eV, which is much lower than the computed formation energy of a C Frenkel pair in both  $Ti_3AlC_2$  and  $Ti_3SiC_2$  ( $>3$  eV) [32]. As such, the equilibrium C Frenkel concentration will be significantly higher.

Both the Al and the Nb interstitials prefer the  $(\frac{2}{3}, \frac{1}{3}, \frac{1}{4})$  site, which is not coordinated in the z-direction by Nb atoms. The Frenkel pair formation energies for Al and Nb are 4.28 eV and 7.56 eV, respectively. Given that Al interstitials preferentially sit within the A-layer (Supplementary Fig. S4g), it is expected that

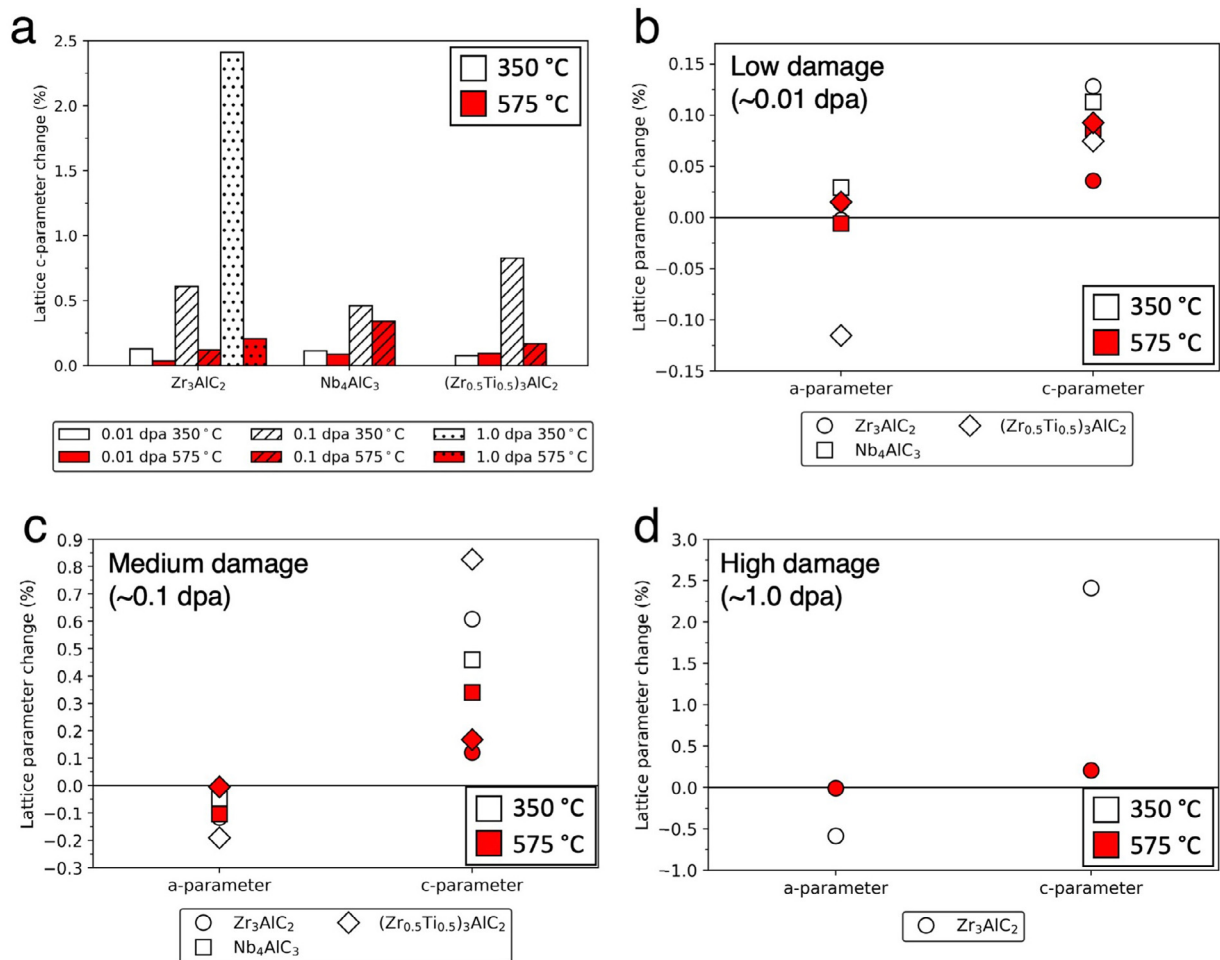
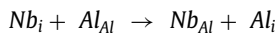


**Fig. 6.** Magnitude of lattice parameter change for Zr<sub>3</sub>AlC<sub>2</sub>, Nb<sub>4</sub>AlC<sub>3</sub> and (Zr<sub>0.5</sub>Ti<sub>0.5</sub>)<sub>3</sub>AlC<sub>2</sub> after proton irradiation of: (a) samples irradiated to both low and moderate damage levels, plus Zr<sub>3</sub>AlC<sub>2</sub> irradiated to a high-damage (~1 dpa) level, showing c-parameter change only, (b) samples irradiated to both low damage (0.01 dpa) and (c) samples irradiated to moderate damage (0.1 dpa). (d) shows lattice parameter changes for Zr<sub>3</sub>AlC<sub>2</sub> after irradiation to a high-damage (~1 dpa) level.

defect recombination will be rapid [32]. The following reaction considering Nb interstitials is predicted to proceed favourably with an energy of  $-0.32$  eV:



This means that Nb interstitials (Nb<sub>i</sub>) associated with Frenkel pair formation are likely to displace an Al atom from its site (Al<sub>Al</sub>) and reside on the Al site (Nb<sub>Al</sub>), creating an Al interstitial (Al<sub>i</sub>). An Al interstitial (expected to be highly mobile in the Al layer) will strongly react with aNb vacancy producing Al<sub>Nb</sub> with an energy of 3.61 eV. This suggests that NbFrenkel pair formation will lead to anti-site defect formation, similar to both Nb<sub>Al</sub> and Al<sub>Nb</sub>.

The anti-site defect formation energies in Nb<sub>4</sub>AlC<sub>3</sub> have also been considered. The preferred Nb site for Al to reside at lies furthest from the A-layer, on the M-2 layer, by a small energy of 0.02 eV (Supplementary Fig. S4h). As such, there is no significant site preference. The Nb:Al anti-site energy is 3.63 eV, similar to the M:A anti-site energy in Ti<sub>3</sub>AlC<sub>2</sub> (~3.3 eV) and Ti<sub>3</sub>SiC<sub>2</sub> [32]. Both Al:C and Nb:C anti-site formation energies are highly unfavourable: 9.53 eV and 12.92 eV, respectively.

Under equilibrium conditions, the dominant radiation-induced defect considered in this work is the C Frenkel pair. However, the ease of defect recombination under irradiation determines the quantity of residual defects responsible for radiation-induced material degradation. As C Frenkel pairs are expected to be extremely difficult to annihilate within the 413-MAX phase structure, one can

expect them to provide a significant contribution to the residual defect population. In addition to C Frenkel pairs, the M:A anti-site pair will not recombine readily, as discussed in previous work on 312-MAX phases [41]. Since Al can reside in the M-2 layer, furthest from the A-layer without a penalty; the recombination of an M:A anti-site pair in Nb<sub>4</sub>AlC<sub>3</sub> is even less favoured, further increasing the population of anti-site pairs.

### 3.4.2. Zr<sub>3</sub>AlC<sub>2</sub>

Zr<sub>3</sub>AlC<sub>2</sub> was considered next and the pristine, non-irradiated condition is shown in Supplementary Fig. S4a. The analysis of the Zr-based 312-MAX lattices showed that only the M-sites have two symmetrically distinct positions. It was again found that Zr vacancies are more stable in the layer closest to the Al layer (by a significant  $-1.99$  eV). Similarly, all intrinsic interstitials were found to be significantly more stable in the A-layer. Both the Zr and C interstitials preferentially reside at the (2/3, 1/3, 1/4) site, coordinated by Zr atoms in the z-direction (similar to C in the Nb<sub>4</sub>AlC<sub>3</sub> structure). Al interstitials preferentially reside in the (1/3, 2/3, 1/4) site which is not coordinated by Zr atoms in the z-direction. Alternative sites in the A-layer are 0.72 eV, 1.76 eV and 0.09 eV less favourable, for Zr, Al and C, respectively. C interstitials between the A and M layers are 1.2 eV less favourable than the preferential site. All other sites in the Zr-C layers for Zr, Al and C are more than 5 eV less favourable as compared to the most favourable site in the A-layer.

The lowest energy Frenkel pair formation energies for Zr, Al and C are 6.66 eV, 1.51 eV and 3.32 eV, respectively (similar to energies reported in [14]). Unlike the Nb<sub>4</sub>AlC<sub>3</sub> system, the lowest energy Frenkel pair is the A Frenkel (Supplementary Fig. S4c) and the energy for the C Frenkel (Supplementary Fig. S4b) is much higher (more similar to C Frenkel formation energies in Ti<sub>3</sub>SiC<sub>2</sub> and Ti<sub>3</sub>AlC<sub>2</sub>). Zr interstitials formed through Frenkel processes will displace Al from its site with an energy of −0.52 eV (similar to Nb in Nb<sub>4</sub>AlC<sub>3</sub>), thus creating mobile Al interstitials in the A-layer. These Al interstitials will react with Zr vacancies (with an energy of 2.70 eV), producing an M:A antisite pair in a similar manner to Nb<sub>4</sub>AlC<sub>3</sub>.

The anti-site formation energies in Zr<sub>3</sub>AlC<sub>2</sub> are similar to those in Nb<sub>4</sub>AlC<sub>3</sub> and other MAX phases. The M:A anti-site (Supplementary Fig. S4d) formation energy is 3.44 eV. However, the Al preferentially resides on an M-1 layer site, which is closest to the A-layer (unlike Nb<sub>4</sub>AlC<sub>3</sub>). The Al has a significant preference to this Zr site (1.39 eV), which again is different to the Nb<sub>4</sub>AlC<sub>3</sub> system. The Al:C and Zr:C anti-site formation energies are highly unfavourable, at 8.38 eV and 10.34 eV, respectively.

As already mentioned, under equilibrium conditions, Al Frenkel pairs will dominate in Zr<sub>3</sub>AlC<sub>2</sub>. Under displacive irradiation conditions, M:A anti-sites and C Frenkel pairs will constitute the majority of the residual defects. Compared to Nb<sub>4</sub>AlC<sub>3</sub>, the density of residual M:A anti-site pairs is expected to be lower in Zr<sub>3</sub>AlC<sub>2</sub>, as a result of their simpler annihilation route. Additionally, the single symmetrically distinct C site in the Zr<sub>3</sub>AlC<sub>2</sub> structure will enable C Frenkel pairs to more readily annihilate as compared to the more complicated structure in Nb<sub>4</sub>AlC<sub>3</sub>. The easier defect annihilation in 312 Zr-based MAX phases in comparison to Nb<sub>4</sub>AlC<sub>3</sub> explains the large unit cell distortion observed experimentally in the Nb<sub>4</sub>AlC<sub>3</sub> when irradiated at 575 °C (Fig. 6).

### 3.5. VT-XRD analysis of AR and proton-irradiated material

In order to validate the findings of the DFT study and demonstrate variability of defect-recovery rates between the 312 and 413-MAX phase structures, analysis of the Zr<sub>3</sub>AlC<sub>2</sub> and Nb<sub>4</sub>AlC<sub>3</sub> ceramics in the AR condition and the low-damage condition (~0.01 dpa) after irradiation at 350 °C was performed using variable temperature VT-XRD. It was possible to observe defect annihilation through a reduction in the rate of thermally-induced lattice parameter expansion.

Fig. 7a demonstrates the reduction in the Zr<sub>3</sub>AlC<sub>2</sub> *a*-parameter values after the low-damage irradiation at 350 °C relative to the AR state throughout the entire temperature range of the heat treatment (i.e. RT – 600 °C). A slight reduction is observed in both the AR and proton-irradiated Zr<sub>3</sub>AlC<sub>2</sub> *a*-parameters from their initial values when the heat-treatment has ceased and the samples are cooled back to room temperature (white markers on Fig. 7a). This suggests that regardless of the condition of the sample, Zr<sub>3</sub>AlC<sub>2</sub> undergoes an inherent reduction in the *a*-parameter upon heat-treatment. By assessing the linear portion of the AR Zr<sub>3</sub>AlC<sub>2</sub> VT-XRD data, the *a*-parameter thermal expansion coefficient (CTE) is calculated as  $7.6 \times 10^{-6} \text{K}^{-1}$ .

Changes in the Zr<sub>3</sub>AlC<sub>2</sub> *c*-parameter measured using VT-XRD demonstrated that in both the AR and low-damage conditions, a plateau occurs in the absolute *c*-parameter expansion above ~400 °C (Fig. 7b). In the low-damage case, this could be attributed to significant defect recovery, as atomic mobility increases at elevated temperatures. This is in agreement with the lattice parameter data measured using XRD at RT, which showed that all irradiations carried out at 575 °C resulted in a reduced *c*-parameter expansion in Zr<sub>3</sub>AlC<sub>2</sub> (Fig. 6), presumably due to greater defect recovery at this temperature. The *c*-parameter CTE for Zr<sub>3</sub>AlC<sub>2</sub> was calculated to be  $9.5 \times 10^{-6} \text{K}^{-1}$ , based on the AR linear data. By

extrapolating the linear trend in thermal expansion to 600 °C in the low-damage Zr<sub>3</sub>AlC<sub>2</sub> case, it is calculated that 0.23% recovery in lattice parameter occurs as a result of annealing. The reasons for the observed *c*-parameter plateau in the AR material, however, is less readily apparent. When extrapolating the thermal expansion to 600 °C in the AR case, lattice recovery is reduced to 0.14%, since there are no irradiation-induced defects to annihilate in this condition.

Interestingly, (Zr<sub>0.5</sub>Ti<sub>0.5</sub>)<sub>3</sub>AlC<sub>2</sub> does not exhibit a plateau in either the *a* or *c* lattice parameter in the AR condition (Fig. 7c and d). It is believed that the N<sub>2</sub> purge used during the experiment led to the destabilisation of the Zr<sub>3</sub>AlC<sub>2</sub> MAX phase. The addition of Ti to the (Zr<sub>0.5</sub>Ti<sub>0.5</sub>)<sub>3</sub>AlC<sub>2</sub> led to the stabilisation of the MAX phase, as demonstrated during its synthesis [15], preventing its decomposition. Therefore, part of the plateauing effect observed in the *c*-parameters of both AR and irradiated Zr<sub>3</sub>AlC<sub>2</sub> (Fig. 7b) is due to the decomposition of this MAX phase. Unfortunately, due to experimental issues, the irradiated (Zr<sub>0.5</sub>Ti<sub>0.5</sub>)<sub>3</sub>AlC<sub>2</sub> was not available for comparison and it is, therefore, impossible to distinguish the contributions of annealing versus decomposition to the *c*-parameter contraction.

Unlike Zr<sub>3</sub>AlC<sub>2</sub>, the VT-XRD study of the *a*-parameter in the AR and proton-irradiated Nb<sub>4</sub>AlC<sub>3</sub> showed no observable differences between the two conditions (Fig. 7e). The CTE of the Nb<sub>4</sub>AlC<sub>3</sub> *a*-parameter was calculated to be  $7.0 \times 10^{-6} \text{K}^{-1}$ . Differences in the expansion of the Nb<sub>4</sub>AlC<sub>3</sub> *c*-parameter between the AR and low-damage states were more readily apparent from the VT-XRD data (Fig. 7f). The Nb<sub>4</sub>AlC<sub>3</sub> *c*-parameter was typically increased by 0.11(3)% across the RT – 550 °C temperature range, in excellent agreement with the XRD data measured at RT (Fig. 6a and b). Even up to 600 °C, the *c*-parameter change in both the AR and low-damage states remained linear (Fig. 7f), with little deviation from the calculated *c*-parameter CTE of  $5.4 \times 10^{-6} \text{K}^{-1}$ . The lack of significant deviation of the Nb<sub>4</sub>AlC<sub>3</sub> lattice parameters from linearity suggests that defect recovery does not occur readily below 600 °C. This behaviour can be explained with the DFT results presented earlier, whereby defect annihilation is hindered in the 413-MAX phase structure as compared to the 312-MAX phase structure.

As mentioned earlier, both Zr<sub>3</sub>AlC<sub>2</sub> and Nb<sub>4</sub>AlC<sub>3</sub> experienced a reduction in the final RT (post-annealing) *a*- and *c*-parameters in both the AR and irradiated states (white markers on Fig. 7). The magnitude of *c*-parameter reduction in the Nb<sub>4</sub>AlC<sub>3</sub> AR and low-damage cases are equal, which suggests that a relief of the residual stresses generated during sample synthesis occurs during post-fabrication annealing (Fig. 7f). These residual compressive strains within the AR material, likely arise during hot-pressing [12]. It is clear, however, that irradiation-induced defect recovery in Nb<sub>4</sub>AlC<sub>3</sub> is limited to temperatures above 600 °C as opposed to Zr<sub>3</sub>AlC<sub>2</sub>, which is capable of dynamic defect recovery above 400 °C. This means that both Zr<sub>3</sub>AlC<sub>2</sub> and Nb<sub>4</sub>AlC<sub>3</sub> MAX phase ceramics with non-optimised microstructures (i.e. low phase purity, inadequate grain size control) would be better suited for use in Gen-IV nuclear systems, where the nominal operating temperatures are higher (> 500 °C). It is important to note, that the reduced phase purity of the Zr<sub>3</sub>AlC<sub>2</sub> samples compared to the Nb<sub>4</sub>AlC<sub>3</sub>, could also have an effect on the defect recovery characteristics between the two. This could occur by way of providing a greater number of grain and phase boundaries for radiation damage to anneal to in Zr<sub>3</sub>AlC<sub>2</sub>. However, the phase-specific study enabled through the use of XRD and large grains, several microns of size, within these structures will likely mitigate such effects. Future efforts should be focussed on producing phase pure Zr<sub>3</sub>AlC<sub>2</sub> in order to confirm that the influence such effects is minimal in further irradiation performance analysis.

The VT-XRD analysis of these ceramics provided information on phase fraction changes during heat treatment (HT). As

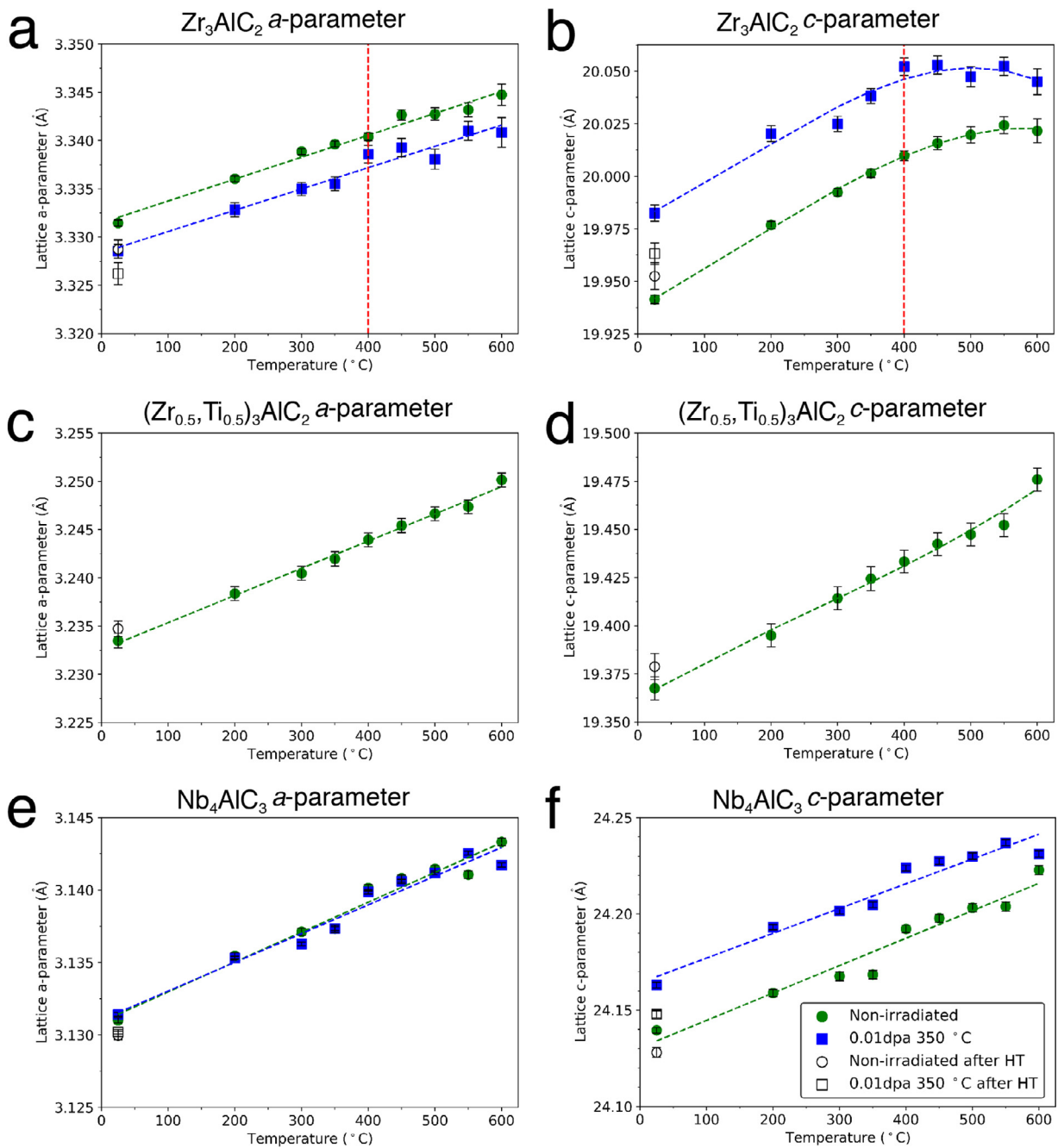


**Fig. 7.** Lattice parameters measured using XRD during the in situ heating of  $Zr_3AlC_2$  and  $Nb_4AlC_3$  in the AR and low damage state ( $\sim 0.01$  dpa) after irradiation at  $350^\circ C$  and of  $(Zr_{0.5}, Ti_{0.5})_3AlC_2$  in the AR state only. Changes in (a) the  $Zr_3AlC_2$   $a$ -parameter and (b)  $Zr_3AlC_2$   $c$ -parameter, as defects are annihilated above  $400^\circ C$  (indicated by the red dashed lines). Changes in (c) the  $a$ -parameter of  $(Zr_{0.5}, Ti_{0.5})_3AlC_2$  and (d) the  $c$ -parameter of  $(Zr_{0.5}, Ti_{0.5})_3AlC_2$  in AR state. Changes in (e) the  $a$ -parameter and (f)  $c$ -parameter of  $Nb_4AlC_3$ , exhibiting little recovery of irradiated lattice parameters. (For interpretation of the references to colour in this figure legend, the reader is referred to the web version of this article.)

discussed earlier, microcracks were observed along the  $c$ -direction in the AR  $Zr_3AlC_2$  MAX phase laths (Fig. 5a). Previous work by Lapauw et al. [12] showed that Al is depleted along these cracks, suggesting a loss of Al during processing. The VT-XRD findings provide an insight as to why such Al leaching occurs above  $300^\circ C$ . Here, the AR  $Zr_3AlC_2$  MAX phase decomposes according to the reaction:  $Zr_3AlC_2 \rightarrow ZrC + Zr_3Al_2$  (Fig. 8a). This process effectively leads to MAX phase exfoliation, forming alternating layers of the binary carbide and the Zr-Al intermetallic. The  $Zr_3AlC_2$  decomposition occurred at a significantly lower temperature than the  $1575^\circ C$  reached during processing [12], suggesting the thermodynamic instability of this particular MAX phase, which may be

exacerbated by the presence of a  $N_2$ -rich atmosphere. This thermodynamic instability may also explain, to a certain extent, the low MAX phase yields in the  $Zr_3AlC_2$  ceramic reported previously [11,12,14]. This phase decomposition also affects the  $Zr_3AlC_2$  lattice parameters and may be responsible for the plateau of the AR  $Zr_3AlC_2$   $c$ -parameter above  $400^\circ C$  (Fig. 7b). Elements will migrate from the MAX phase to the decomposition products, resulting in a reduction in  $c$ -parameter in the remaining non-stoichiometric MAX phase. However, inspection of the XRD data indicates that the  $Zr_3AlC_2$ , proton-irradiated to both moderate and high damage levels, at both  $350$  and  $575^\circ C$ , only reduces in MAX phase fraction by approximately 1 – 5 wt.% in all cases. This is dramatically

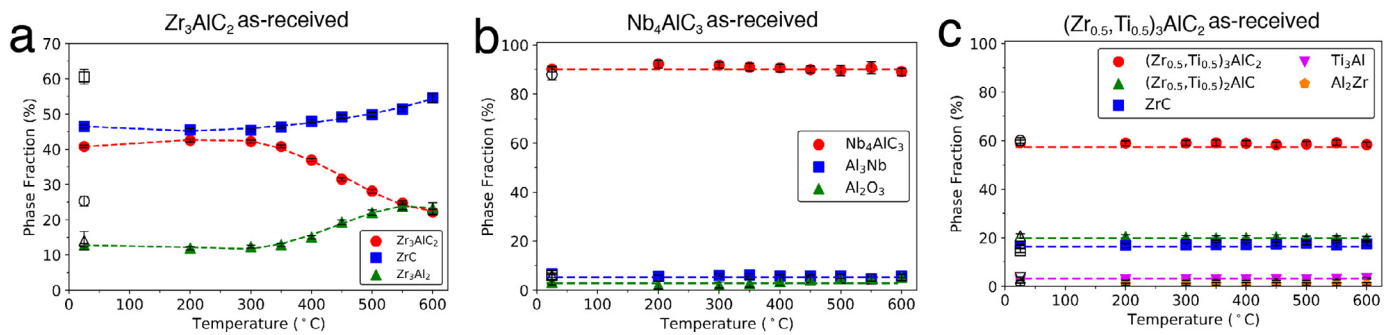


**Fig. 8.** Phase changes observed during the XRD in situ heating experiment in the non-irradiated AR sample. (a)  $Zr_3AlC_2$ ; (b)  $Nb_4AlC_3$ ; (c)  $(Zr_{0.5},Ti_{0.5})_3AlC_2$ . White markers indicate phase fractions after cooling back to room temperature.

lower than the decomposition indicated by the VT-XRD. As alluded to earlier, it is believed that the  $N_2$ -rich environment is a cause for such changes, leading to the destabilisation of  $Zr_3AlC_2$ . In the case of  $(Zr_{0.5},Ti_{0.5})_3AlC_2$ , which is stabilised by the addition of Ti, such phase decomposition is not observed (Fig. 8c). The lack of oxide/nitride peaks in the  $Zr_3AlC_2$  VT-XRD data indicates that the  $N_2$ -rich environment leads to a decomposition of the MAX phase without the precipitation of nitride phases.

On the other hand,  $Nb_4AlC_3$  demonstrated phase stability across the entire temperature range, up to 600 °C (Fig. 8b). An average  $Nb_4AlC_3$  fraction of 90.3(2) wt.% was measured. This inherent thermal stability and resistance to Al leaching, leads to reduced micro-cracking severity in this ceramic (Fig. 5d). It should also be noted that ~5.8(5) wt.% of an  $Al_3Nb$  intermetallic is present throughout the HT of AR  $Nb_4AlC_3$ , but does not increase in fraction. A 3.7(12) wt.%  $Al_2O_3$  fraction is also observed (Fig. 8b), which was not detected in the XRD analysis of  $Nb_4AlC_3$  at RT (Supplementary Fig. S3b), and is attributed to the microstructural heterogeneity of the material. The  $Al_2O_3$  is present in the AR  $Nb_4AlC_3$  as observed previously in similar compositions [13].

#### 4. Conclusions

This investigation has provided an initial insight into the suitability of the three new MAX phase compositions;  $Zr_3AlC_2$ ,  $(Zr_{0.5},Ti_{0.5})_3AlC_2$  and  $Nb_4AlC_3$  for use in ATF applications or future Gen-IV reactor designs. The analysis of proton irradiated MAX phase ceramics shows that the  $Zr_3AlC_2$  offers a superior ability for irradiation-induced defect recovery above temperatures of 400 °C compared to  $Nb_4AlC_3$ .

Such limited low-temperature defect-recovery leads to cracking of the MAX phases as witnessed in this study. The use of DFT has shown that 413-MAX phases in general may not perform well under low-temperature irradiation conditions, due to the preference for M:A antisites and C Frenkel pairs to form at the M-2 layer, furthest from the A-layer, presenting a significant barrier for defect recombination. However, despite these drawbacks, the 413-MAX  $Nb_4AlC_3$  demonstrates a greater phase stability in a  $N_2$ -rich environment compared to the 312-MAX  $Zr_3AlC_2$ , which undergoes phase decomposition at temperatures above 400 °C. The addition of Ti to the  $(Zr_{0.5},Ti_{0.5})_3AlC_2$  composition, stabilises the MAX phase in such an environment. In general, the low yields of  $Zr_3AlC_2$  MAX phase during fabrication may impede its wider use.

This study suggests that these particular MAX phase compositions are better suited to future generation nuclear applications, involving higher operating temperatures. As future Gen-IV reactors will operate at temperatures above 500 °C, the more stable  $Nb_4AlC_3$  may demonstrate a favourable defect-recovery ability under these conditions. Due to the poor ability for defect-recombination in the 413-MAX phases, compared to the 312-MAX

phases, established in this study, further high-damage and high-temperature irradiation experiments are required. This will allow an understanding of whether the irradiation behaviour of the 413-MAX phases will be a significant limiting factor for the use of such compositions in future nuclear reactor environments.

#### Declaration of Competing Interest

None

#### Acknowledgments

The authors wish to thank the EPSRC-funded Carbides for Future Fission Environments (CaFFE) project (EP/M018482/1). We acknowledge the support of The University of Manchester's Dalton Cumbrian Facility (DCF), a partner in the National Nuclear User Facility, the EPSRC UK National Ion Beam Centre and the Henry Royce Institute. Thanks to B. Tunca for her support with SEM imaging of the irradiated (Zr,Ti)-312 samples. We recognise Dr. A. Smith and Dr. P. Wady for their assistance during the irradiations. The authors also wish to thank M. Topping, M. Rogers, A. Garner, A. Smith, X. Xu, S. Irukuvarghula, D. Lunt, R. Jones and C. Gillen for their support in staffing shifts during the irradiations. Special thanks to Dr. J. Warren and Mr. H. Chen for their assistance with the XRD analysis.

#### Funding

This work was funded by the Carbides for Future Fission Environments (CaFFE) project under grant number EP/M018482/1. SCM is supported by the Sêr Cymru II through the Welsh European Funding Office. KL acknowledges funding from the Euratom research and training program 2014–18 under grant agreement No. 740415 (H2020 IL TROVATORE). MP acknowledges EPSRC funding for his leadership fellowship (EP/I005420/1).

#### Supplementary materials

Supplementary material associated with this article can be found, in the online version, at doi:10.1016/j.actamat.2019.10.049.

#### References

- [1] E.N. Hoffman, D.W. Vinson, R.L. Sindelar, D.J. Tallman, G. Kohse, M.W. Barsoum, MAX phase carbides and nitrides: properties for future nuclear power plant in-core applications and neutron transmutation analysis, *Nuclear Eng. Des.* 244 (2012) 17–24, doi:10.1016/j.nucengdes.2011.12.009.
- [2] W.E. Lee, M. Gilbert, S.T. Murphy, R.W. Grimes, Opportunities for advanced ceramics and composites in the nuclear sector, *J. Am. Ceram. Soc.* 96 (2013) 2005–2030, doi:10.1111/jace.12406.
- [3] M.W. Barsoum, MAX Phases, Wiley-VCH Verlag GmbH & Co. KGaA, Weinheim, Germany, 2013, doi:10.1002/9783527654581.

- [4] M.W. Barsoum, M. Radovic, Elastic and mechanical properties of the MAX phases, *Annu. Rev. Mater. Res.* 41 (2011) 195–227, doi:[10.1146/annurev-matsci-062910-100448](https://doi.org/10.1146/annurev-matsci-062910-100448).
- [5] D.J. Tallman, L. He, B.L. Garcia-Diaz, E.N. Hoffman, G. Kohse, R.L. Sindelar, et al., Effect of neutron irradiation on defect evolution in  $\text{Ti}_3\text{SiC}_2$  and  $\text{Ti}_2\text{AlC}$ , *J. Nuclear Mater.* 468 (2016) 194–206, doi:[10.1016/j.jnucmat.2015.10.030](https://doi.org/10.1016/j.jnucmat.2015.10.030).
- [6] D.J. Tallman, L. He, J. Gan, E.N. Caspi, E.N. Hoffman, M.W. Barsoum, Effects of neutron irradiation of  $\text{Ti}_3\text{SiC}_2$  and  $\text{Ti}_3\text{AlC}_2$  in the 121–1085°C temperature range, *J. Nuclear Mater.* 484 (2017) 120–134, doi:[10.1016/j.jnucmat.2016.11.016](https://doi.org/10.1016/j.jnucmat.2016.11.016).
- [7] C. Ang, C. Silva, C. Shih, T. Koyanagi, Y. Katoh, S.J. Zinkle, Anisotropic swelling and microcracking of neutron irradiated  $\text{Ti}_3\text{AlC}_2$ – $\text{Ti}_5\text{Al}_2\text{C}_3$  materials, *Scr. Mater.* 114 (2016) 74–78, doi:[10.1016/j.scriptamat.2015.11.008](https://doi.org/10.1016/j.scriptamat.2015.11.008).
- [8] U.S. DoE, A technology roadmap for generation IV nuclear energy systems, *Nuclear Energy Res. Adv. Comm. Generat. IV Int. Forum* (2002), doi:[10.2172/859029](https://doi.org/10.2172/859029).
- [9] F. Onimus, J.L. Béchade, *Radiation Effects in Zirconium Alloys, Comprehensive Nuclear Materials, 2012 Amsterdam*.
- [10] P. Rodriguez, *Nuclear Reactor Materials: Irradiation Effects*, Elsevier, 2001, doi:[10.1016/b0-08-043152-6/01124-4](https://doi.org/10.1016/b0-08-043152-6/01124-4).
- [11] T. Lapauw, K. Lambrinou, T. Cabioch, J. Halim, J. Lu, A. Pesach, et al., Synthesis of the new MAX phase  $\text{Zr}_2\text{AlC}$ , *J. Eur. Ceram. Soc.* 36 (2016) 1847–1853, doi:[10.1016/j.jeurceramsoc.2016.02.044](https://doi.org/10.1016/j.jeurceramsoc.2016.02.044).
- [12] T. Lapauw, J. Halim, J. Lu, T. Cabioch, L. Hultman, M.W. Barsoum, et al., Synthesis of the novel  $\text{Zr}_3\text{AlC}_2$  MAX phase, *J. Eur. Ceram. Soc.* 36 (2015) 1–5, doi:[10.1016/j.jeurceramsoc.2015.10.011](https://doi.org/10.1016/j.jeurceramsoc.2015.10.011).
- [13] T. Lapauw, D. Tytko, K. Vanmeensel, S. Huang, P.-P. Choi, D. Raabe, et al., ( $\text{Nb}_x$ ,  $\text{Zr}_{1-x}$ ) $\text{AlC}_3$  MAX phase solid solutions: processing, mechanical properties, and density functional theory calculations, *Inorg. Chem.* 55 (2016) 5445–5452, doi:[10.1021/acs.inorgchem.6b00484](https://doi.org/10.1021/acs.inorgchem.6b00484).
- [14] E. Zapata-Solvas, S.-R.G. Christopoulos, N. Ni, D.C. Parfitt, D. Horlait, M.E. Fitzpatrick, et al., Experimental synthesis and density functional theory investigation of radiation tolerance of  $\text{Zr}_3(\text{Al}_{1-x}\text{Si}_x)_2\text{C}_2$  MAX phases, *J. Am. Ceram. Soc.* 2 (2017) 27–11, doi:[10.1111/jace.14742](https://doi.org/10.1111/jace.14742).
- [15] E. Zapata-Solvas, M.A. Hadi, D. Horlait, D.C. Parfitt, A. Thibaud, A. Chroneos, et al., Synthesis and physical properties of ( $\text{Zr}_{1-x}\text{Ti}_x$ ) $\text{AlC}_2$  MAX phases, *J. Am. Ceram. Soc.* 2 (2017) 27, doi:[10.1111/jace.14870](https://doi.org/10.1111/jace.14870).
- [16] L.L. Snead, Y. Katoh, S. Kondo, Effects of fast neutron irradiation on zirconium carbide, *J. Nuclear Mater.* 399 (2010) 200–207, doi:[10.1016/j.jnucmat.2010.01.020](https://doi.org/10.1016/j.jnucmat.2010.01.020).
- [17] Y. Katoh, G. Vasudevamurthy, T. Nozawa, L.L. Snead, Properties of zirconium carbide for nuclear fuel applications, *J. Nuclear Mater.* 441 (2013) 718–742, doi:[10.1016/j.jnucmat.2013.05.037](https://doi.org/10.1016/j.jnucmat.2013.05.037).
- [18] D.J. Tallman, E.N. Hoffman, E.N. Caspi, B.L. Garcia-Diaz, G. Kohse, R.L. Sindelar, et al., Effect of neutron irradiation on select MAX phases, *Acta Mater.* 85 (2015) 132–143, doi:[10.1016/j.actamat.2014.10.068](https://doi.org/10.1016/j.actamat.2014.10.068).
- [19] K.R. Whittle, M.G. Blackford, R.D. Aughterson, S. Moricca, G.R. Lumpkin, D.P. Riley, et al., Radiation tolerance of  $\text{M}_{n+1}\text{AX}_n$  phases,  $\text{Ti}_3\text{AlC}_2$  and  $\text{Ti}_3\text{SiC}_2$ , *Acta Mater.* 58 (2010) 4362–4368, doi:[10.1016/j.actamat.2010.04.029](https://doi.org/10.1016/j.actamat.2010.04.029).
- [20] J.C. Nappé, C. Maurice, P. Grosseau, F. Audubert, Microstructural changes induced by low energy heavy ion irradiation in titanium silicon carbide, *J. Eur. Ceram. Soc.* 31 (2011) 1503–1511, doi:[10.1016/j.jeurceramsoc.2011.01.002](https://doi.org/10.1016/j.jeurceramsoc.2011.01.002).
- [21] M.K. Patel, D.J. Tallman, J.A. Valdez, J. Aguiar, O. Anderoglu, M. Tang, et al., Effect of helium irradiation on  $\text{Ti}_3\text{AlC}_2$  at 500°C, *Scr. Mater.* 77 (2014) 1–4, doi:[10.1016/j.scriptamat.2013.12.010](https://doi.org/10.1016/j.scriptamat.2013.12.010).
- [22] M. Bugnet, T. Cabioch, V. Mauchamp, P. Guérin, M. Marteau, M. Jaouen, Stability of the nitrogen-deficient  $\text{Ti}_2\text{AlN}_x$  MAX phase in  $\text{Ar}^{2+}$ -irradiated ( $\text{Ti}_x\text{Al}$ ) $\text{Ti}_2\text{AlN}_x$  multilayers, *J. Mater. Sci.* 45 (2010) 5547–5552, doi:[10.1007/s10853-010-4615-0](https://doi.org/10.1007/s10853-010-4615-0).
- [23] M. Le Flem, X. Liu, S. Doriot, T. Cozzika, I. Monnet, Irradiation damage in  $\text{Ti}_3(\text{Si,Al})\text{C}_2$ : a TEM investigation, *Int. J. Appl. Ceramic Technol.* 7 (2010) 766–775, doi:[10.1111/j.1744-7402.2010.02523.x](https://doi.org/10.1111/j.1744-7402.2010.02523.x).
- [24] C. Ang, S. Zinkle, C. Shih, C. Silva, N. Cetiner, Y. Katoh, Phase stability, swelling, microstructure and strength of  $\text{Ti}_3\text{SiC}_2$ – $\text{TiC}$  ceramics after low dose neutron irradiation, *J. Nuclear Mater.* 483 (2017) 44–53, doi:[10.1016/j.jnucmat.2016.10.036](https://doi.org/10.1016/j.jnucmat.2016.10.036).
- [25] S. Liu, C. Wang, T. Yang, Y. Fang, Q. Huang, Y. Wang, High temperature effects on irradiation damage of  $\text{Ti}_2\text{AlC}$ , *Nuclear Inst. Methods Phys. Res. Sect. B: Beam Interact. Mater. Atoms* 406 (2017) 662–669, doi:[10.1016/j.nimb.2017.01.040](https://doi.org/10.1016/j.nimb.2017.01.040).
- [26] J.C. Nappé, I. Monnet, P. Grosseau, F. Audubert, B. Guilhot, M. Beauvy, et al., Structural changes induced by heavy ion irradiation in titanium silicon carbide, *J. Nuclear Mater.* 409 (2011) 53–61, doi:[10.1016/j.jnucmat.2010.12.235](https://doi.org/10.1016/j.jnucmat.2010.12.235).
- [27] G.S. Was, *Fundamentals of Radiation Materials Science: Metals and Alloys*, Springer Berlin Heidelberg, Berlin, Heidelberg, 2007, doi:[10.1007/978-3-540-49472-0](https://doi.org/10.1007/978-3-540-49472-0).
- [28] S.J. Zinkle, L.L. Snead, Opportunities and limitations for ion beams in radiation effects studies: bridging critical gaps between charged particle and neutron irradiations, *Scr. Mater.* 143 (2018) 154–160, doi:[10.1016/j.scriptamat.2017.06.041](https://doi.org/10.1016/j.scriptamat.2017.06.041).
- [29] J. Schindelin, I. Arganda-Carreras, E. Frise, V. Kaynig, M. Longair, T. Pietzsch, et al., Fiji: an open-source platform for biological-image analysis, *Nat. Methods* 9 (2012) 676–682, doi:[10.1038/nmeth.2019](https://doi.org/10.1038/nmeth.2019).
- [30] G. Kresse, J. Hafner, Ab initio molecular-dynamics simulation of the liquid-metal–amorphous–semiconductor transition in germanium, *Phys. Rev. B* 49 (1994) 14251–14269, doi:[10.1103/PhysRevB.49.14251](https://doi.org/10.1103/PhysRevB.49.14251).
- [31] G. Kresse, J. Furthmüller, Efficiency of ab-initio total energy calculations for metals and semiconductors using a plane-wave basis set, *Comput. Mater. Sci.* 6 (1996) 15–50, doi:[10.1016/0927-0256\(96\)00008-0](https://doi.org/10.1016/0927-0256(96)00008-0).
- [32] S.C. Middleburgh, G.R. Lumpkin, D. Riley, Accommodation, accumulation, and migration of defects in  $\text{Ti}_3\text{SiC}_2$  and  $\text{Ti}_3\text{AlC}_2$  MAX phases, *J. Am. Ceram. Soc.* 96 (2013) 3196–3210, doi:[10.1111/jace.12537](https://doi.org/10.1111/jace.12537).
- [33] P.E. Blöchl, Projector augmented-wave method, *Phys. Rev. B* 50 (1994) 17953–17979, doi:[10.1103/PhysRevB.50.17953](https://doi.org/10.1103/PhysRevB.50.17953).
- [34] J.P. Perdew, K. Burke, M. Ernzerhof, Generalized gradient approximation made simple, *Phys. Rev. Lett.* 77 (1996) 3865–3868, doi:[10.1103/PhysRevLett.77.3865](https://doi.org/10.1103/PhysRevLett.77.3865).
- [35] P.T. Wady, A. Draude, S.M. Shubeita, A.D. Smith, N. Mason, S.M. Pimblott, et al., Accelerated radiation damage test facility using a 5MV tandem ion accelerator, *Nuclear Inst. Methods Phys. Res. A* 806 (2016) 109–116, doi:[10.1016/j.nima.2015.09.088](https://doi.org/10.1016/j.nima.2015.09.088).
- [36] J.F. Ziegler, M.D. Ziegler, J.P. Biersack, SRIM – The stopping and range of ions in matter (2010), *Nuclear Inst. Methods Phys. Res. Sect. B: Beam Interact. Mater. Atoms* 268 (2010) 1818–1823, doi:[10.1016/j.nimb.2010.02.091](https://doi.org/10.1016/j.nimb.2010.02.091).
- [37] J. Liu, R.E. Saw, Y.H. Kiang, Calculation of effective penetration depth in X-ray diffraction for pharmaceutical solids, *J. Pharm. Sci.* 99 (2010) 3807–3814, doi:[10.1002/jps.22202](https://doi.org/10.1002/jps.22202).
- [38] A.A. Coelho, J. Evans, I. Evans, A. Kern, The TOPAS symbolic computation system, 26 (2011) S22–S25, doi:[10.1154/1.3661087](https://doi.org/10.1154/1.3661087).
- [39] B. Tunca, T. Lapauw, O.M. Karakulina, M. Batuk, T. Cabioch, J. Hadermann, et al., Synthesis of MAX phases in the Zr-Ti-Al-C system, *Inorg. Chem.* 56 (2017) 3489–3498, doi:[10.1021/acs.inorgchem.6b03057](https://doi.org/10.1021/acs.inorgchem.6b03057).
- [40] T. El-Raghy, M.W. Barsoum, Processing and mechanical properties of  $\text{Ti}_3\text{SiC}_2$ : I, reaction path and microstructure evolution, *J. Am. Ceram. Soc.* 82 (1999) 2849–2854, doi:[10.1111/j.1151-2916.1999.tb02166.x](https://doi.org/10.1111/j.1151-2916.1999.tb02166.x).
- [41] J. Ward, S. Middleburgh, M. Topping, A. Garner, D. Stewart, M.W. Barsoum, et al., Crystallographic evolution of MAX phases in proton irradiating environments, *J. Nuclear Mater.* 502 (2018) 220–227, doi:[10.1016/j.jnucmat.2018.02.008](https://doi.org/10.1016/j.jnucmat.2018.02.008).
- [42] Q. Huang, H. Han, R. Liu, G. Lei, L. Yan, J. Zhou, Saturation of ion irradiation effects in MAX phase  $\text{Cr}_2\text{AlC}$ , *Acta Mater.* 110 (2016) 1–7, doi:[10.1016/j.actamat.2016.03.021](https://doi.org/10.1016/j.actamat.2016.03.021).
- [43] R. Liu, G. Lei, H. Huang, J. Li, S. He, D. Li, et al., Irradiation resistance of MAX phases  $\text{Ti}_3\text{SiC}_2$  and  $\text{Ti}_3\text{AlC}_2$ : characterization and comparison, *J. Nuclear Mater.* 465 (2015) 640–647, doi:[10.1016/j.jnucmat.2015.06.056](https://doi.org/10.1016/j.jnucmat.2015.06.056).
- [44] S.J. Zinkle, L.L. Snead, Designing radiation resistance in materials for fusion energy, *Annu. Rev. Mater. Res.* 44 (2014) 241–267, doi:[10.1146/annurev-matsci-070813-113627](https://doi.org/10.1146/annurev-matsci-070813-113627).
- [45] C. Hu, F. Li, L. He, M. Liu, J. Zhang, J. Wang, et al., In situ reaction synthesis, electrical and thermal, and mechanical properties of  $\text{Nb}_4\text{AlC}_3$ , *J. Am. Ceram. Soc.* 91 (2008) 2258–2263, doi:[10.1111/j.1551-2916.2008.02424.x](https://doi.org/10.1111/j.1551-2916.2008.02424.x).